# Ultralow Thermal Conductivity and Improved Thermoelectric Properties of Al-Doped ZnO by In Situ $O_2$ Plasma Treatment

*Vikesh Sethi, Kai Sun, Daniel Newbrook, Danielle Runacres, Tongjun Zhang, Victoria Greenacre, C. H. (Kees) de Groot, and Ruomeng Huang**

**The thriving of Internet-of-Things and integrated wireless sensor networks has brought an unprecedented demand for sustainable micro-Watt-scale power supplies. Development of high-performing micro-thermoelectric generator (μ-TEG) that can convert waste thermal energy into electricity and provide sustainable micro-Watt-scale power is therefore extremely timely and important. Herein, a significant advance in the development of earth-abundant, nontoxic thermoelectric materials of aluminum-doped zinc oxide (AZO) is presented. Through nanostructure engineering using a novel in situ $O_2$ plasma treatment, AZO films are demonstrated with ultralow thermal conductivity of 0.16 W $m^{-1}$ $K^{-1}$ which is the lowest reported in the literature. This nanostructured film yields a power factor of 294 μW $m^{-1}$ $K^{-2}$ at 563 K and has resulted in a state-of-the-art *ZT* of 0.11 at room temperature and 0.72 at 563 K for AZO thin films. Furthermore, the fabrication and testing of a prototype lateral μ-TEG are reported based on the AZO thin film which achieves a power output of 1.08 nW with an applied temperature difference of 16.9 °C.**

## 1. Introduction

At present, a huge expansion of the Internet-of-Things (IoT) market is taking place, with issues stemming from potential power methods for integrated wireless sensor networks.[1] IoT systems work under the principle of an IoT node or sensor acquiring data, and then transferring this data over a network to be processed for a specific application, with each node operating intermittently and having low energy demands (≈100 μJ $cycle^{-1}$).[2] Common power methods, such as Li-ion batteries, are impractical due to the sheer number of projected IoT nodes which are in excess of 50 billion and increasing at an exponential rate.[2] This has caused a shift to alternative energy harvesting methods to be explored.

Thermoelectric generators are a promising energy-harvesting technology due to their ability of solid-state conversion of heat into electricity. Thermoelectric devices have shown promise for a range of potential applications, including on-chip thermal management,[3] cryotherapy,[4] biomedical sensors,[4] waste heat recovery,[5] space exploration,[6] and wearable electronics.[7,8] It is composed of an alternating arrangement of n-type and p-type thermoelectric materials wired electrically in series and thermally in parallel.[9] The performance of thermoelectric materials is evaluated by a figure of merit commonly referred to as *ZT*, which is shown in Equation (1).

$$ZT = \frac{S^2\sigma}{k}T \tag{1}$$

where $\sigma$ is the electrical conductivity, $S$ is the Seebeck coefficient, and $k$ is the thermal conductivity. A good thermoelectric material requires a high electrical conductivity, a high Seebeck coefficient, and a low thermal conductivity. Materials possessing these characteristics are commonly associated with heavily doped degenerate semiconductors, on which the majority of thermoelectric materials are developed.[10] At present, materials such as $Bi_2Te_3$,[5] PbTe,[11] GeTe,[12] SnSe,[13] skutterudites,[14] half-Heusler,[15] SiGe,[16] and thermoelectric conducting polymers[17] are being explored as potential candidates. The majority of commercial thermoelectric devices on the market are highly reliant on scarce and toxic elements (i.e., Bi, Te and Pb), yielding economic and health concerns.[18,19] Additionally, practical applications of these materials have been restricted by decomposition at low temperatures, material oxidation, and phase transitions.[20] These issues have stimulated research efforts on oxide-based thermoelectric materials such as $Ca_3Co_4O_9$,[21] $CaMnO_3$,[22] $SrTiO_3$,[23] $In_2O_3$,[24] and ITO.[25]

Among those oxides, ZnO is a promising candidate due to its low-cost, natural abundance, nontoxicity, and high chemical and

V. Sethi, K. Sun, D. Newbrook, T. Zhang, C. H. (K.) de Groot, R. Huang
School of Electronics and Computer Science
University of Southampton
Southampton SO17 1BJ, UK
E-mail: r.huang@soton.ac.uk

D. Runacres, V. Greenacre
School of Chemistry
University of Southampton
Southampton SO17 1BJ, UK

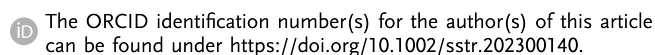
The ORCID identification number(s) for the author(s) of this article can be found under https://doi.org/10.1002/sstr.202300140.

© 2023 The Authors. Small Structures published by Wiley-VCH GmbH. This is an open access article under the terms of the Creative Commons Attribution License, which permits use, distribution and reproduction in any medium, provided the original work is properly cited.

**DOI: 10.1002/sstr.202300140**

thermal stability.[26,27] However, the ionic nature of the bonds formed leads to intrinsically lower carrier mobilities due to electron aggregation around cationic sites and a large thermal conductivity due to the strong ionic nature of oxide bonds.[28] This leads to most strategies for improving the performance of ZnO thin films centered on improving electrical conductivity and reducing thermal conductivity. It was first demonstrated by Ohtaki et al. that the electrical performance of bulk ZnO can be significantly improved with the use of Al doping which increases carrier concentration.[29,30] However, the thermoelectric application of AZO was still hindered by a large thermal conductivity.[29] An effective strategy to reduce thermal conductivity as well as to enhance thermoelectric performance is quantum confinement.[31,32] 2D confinement is an effective method of decoupling the thermoelectric parameters, with the simultaneous improvement of Seebeck and reduction of thermal conductivity.[33,34]

Several works have been devoted to developing thin film AZO via different fabrication methods. Wen et al. deposited AZO thin films using plasma-enhanced DC magnetron sputtering and modulated grain size with the application of an electrode bias to increase plasma density.[35] Saini et al. deposited AZO thin films on fused silica substrates at various deposition temperatures and found that lower temperatures (300 °C) were favorable due to an improved power factor, driven by a larger electrical conductivity.[36] The group also fabricated AZO thin films via mist chemical vapor deposition (MCVD). The films exhibited exceptionally low thermal conductivity of 0.6 $W m^{-1} K^{-1}$ which is driven by the highly porous nature of the films grown. However, the films produced had low electrical conductivities hindering the thermoelectric performance.[37] Park et al. reported similarly low thermal conductivities in samples prepared by sol–gel spinning and found thermal conductivity to decrease with reduced grain sizes, due to enhanced scattering at grain boundaries.[38]

Of the various methods used, a popular deposition method to produce high-quality AZO thin films is atomic layer deposition (ALD). ALD offers nanometer control of film thickness with exceptional uniformity over a large substrate due to the sequential self-limiting surface reactions.[39,40] This method also benefits from a low deposition temperature (<20 °C), which allows for compatibility with a wide range of substrates. Typical ALD depositions of AZO utilize two precursors, diethylzinc (DEZ) and trimethylaluminum (TMA), with the use of water as a reactant.[40,41] This water-based process is commonly termed a thermal ALD process.[42] Plasma-enhanced ALD (PE-ALD) uses $O_2$ plasma as a reactant for AZO growth and has been suggested to possess many benefits when compared to thermal ALD growth, including lower deposition temperatures, lower carbon content, better film adhesion, enhancement of growth characteristics, and alteration of electrical performance.[42–44] Most reports of PE-ALD involve a substrate pretreatment to improve substrate adhesion or an ex situ $O_2$ plasma treatment to modify the electrical and mechanical properties of the film.[42,44] We have previously demonstrated that carrier concentration can be tuned via an in situ $O_2$ plasma treatment on ZnO thin films.[45] However, reports of the effect of in situ $O_2$ plasma treatment on the thermoelectric performance of AZO thin films have yet to be reported.

Herein, we report the deposition and characterization of AZO thin films deposited by in situ $O_2$ PE-ALD. The full thermoelectric properties of our AZO thin films including electrical conductivity, Seebeck coefficient, and thermal conductivity measurements are characterized to calculate the figure-of-merit *ZT*. We go on further to fabricate and test a prototype lateral micro-thermoelectric generator (μ-TEGs) based on the AZO thin film developed in this work in which we obtain encouraging results.

## 2. Results and Discussion

### 2.1. PE-ALD-Deposited AZO Thin Films

The Al-doped ZnO (AZO) thin films were deposited on $Si/SiO_2$ substrates using PE-ALD, using the supercycle shown in **Figure 1**. Each deposition cycle is governed by three processes, namely, a DEZ cycle, a TMA cycle, and an $O_2$ plasma exposure. Each supercycle begins with a DEZ cycle, which is composed of an introduction of DEZ and $H_2O$ to form a layer of ZnO. Each DEZ cycle is followed by an $O_2$ plasma exposure with different exposure times ($t_c = 0, 2, 4, 6$ s) to modulate its properties. These cycles are repeated sequentially 24 times before the TMA cycle giving an Al/Zn cycle ratio of 4%. Cycle ratios can be varied to achieve different doping concentrations and a full supercycle is repeated to reach a target thickness. Gas purges are conducted using Ar after each injection of precursor, removing residual reactants from the chamber. Details of the deposition process can be found in the Experimental Section.

**Figure 2** shows the top-view (top) and cross-sectional (bottom) scanning electron microscopy (SEM) images for the AZO thin films with varying $O_2$ plasma treatment times, (a) $t_c = 0$ s, (b) $t_c = 2$s, (c) $t_c = 4$ s, and (d) $t_c = 6$ s. All films yielded a continuous polycrystalline layer of needle-like structures, which is similar to reports on ALD-grown AZO.[46] The in situ $O_2$ plasma treatment was noted to govern the film's grain orientation, size, and density. The structures appear to systematically translate from seemingly random orientated needle-like grains parallel to the substrate to well-ordered structures perpendicular to the substrate with increasing plasma treatment time ($t_c$). This is more explicitly shown in the cross-sectional images with the formation of nanopillars perpendicular to the substrate becoming more apparent with longer exposure times ($t_c = 4$, 6 s), as indicated by the structures displayed in the boxes shown in Figure 2c,d. This indicates that a sufficient in situ plasma step

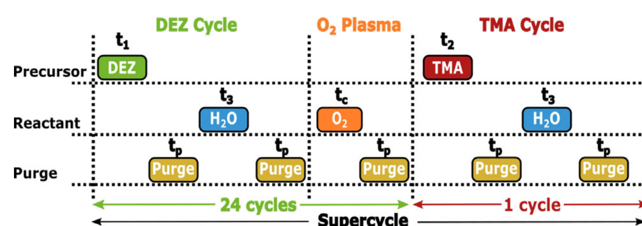


**Figure 1.** A visual depiction of the PE-ALD supercycle used to grow AZO thin films. It is composed of three distinct cycles, namely, DEZ, $O_2$ plasma, and TMA cycles. Each injection of precursor/reactant has a characteristic time associated with the period of the process.


© 2023 The Authors. Small Structures published by Wiley-VCH GmbH
26884062, 0, Downloaded from https://onlinelibrary.wiley.com/doi/10.1002/sstr.202300140 by Test, Wiley Online Library on [26/07/2023]. See the Terms and Conditions (https://onlinelibrary.wiley.com/terms-and-conditions) on Wiley Online Library for rules of use; OA articles are governed by the applicable Creative Commons License

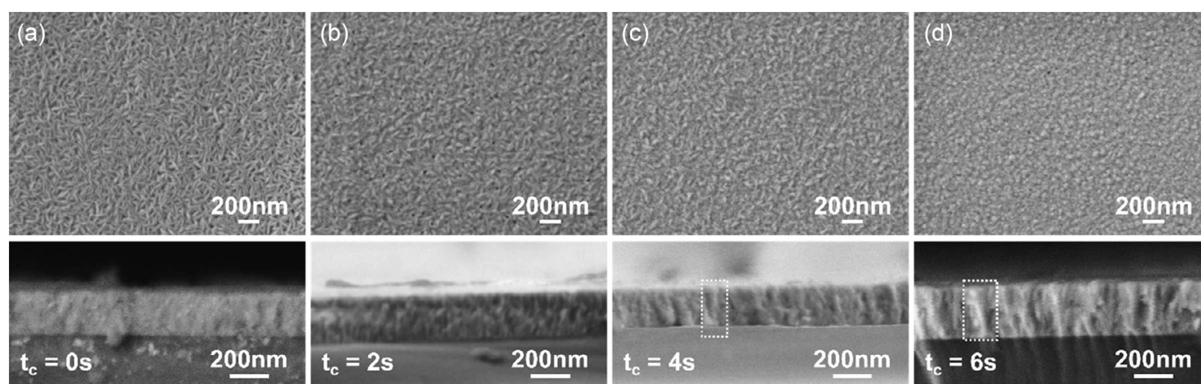


**Figure 2.** Top-view (top) and cross-sectional (bottom) SEM images showing the morphologies of AZO thin films deposited by ALD with in situ $O_2$ plasma treatment times ($t_c$) of a) 0 s, b) 2 s, c) 4 s, and d) 6 s. Boxes have been added to explicitly show the nanopillar formation within the film.

can promote the growth of AZO nanopillars with *c*-axis alignment. The nanopillars observed in the $t_c = 6$ s film appear to be thicker than the pillars formed in the $t_c = 4$ s film, indicating longer plasma treatment time encourages grain coalescence, leading to increased grain size. Furthermore, the formation of pin-holes is significantly suppressed with increasing plasma exposure, which is believed to be due to a higher density of nucleation sites.[47]

**Figure 3** shows the topological and phase contrast atomic force microscopy (AFM) images for all the AZO thin films. Due to the small feature sizes evident from the SEM images displayed in Figure 2, phase contrast imaging was used to reveal the small structures and fine details, which are commonly associated with ALD-grown thin films.[48] The AFM further supports the polycrystalline topology of the AZO thin films with the grain formation consistent with the grain morphologies observed in the SEM images. The grains transform from needle-like structures with seeming random orientations, to very well-ordered pillared structures for prolonged plasma treatment times. It is evident from the larger grain growth observed from the $t_c = 6$ s film, when compared with the $t_c = 4$ s film, that a longer exposure time promotes grain growth. All films yielded smooth topologies with surface roughness around ≈2 nm which is consistent with reports for ALD-grown AZO thin films.[49]

Presented in **Figure 4**a are the X-ray diffraction (XRD) spectra for the four AZO films. The spectra displayed reflections which were consistent with the wurtzite-type ZnO structure with space group symmetry $P6_3mc$.[50,51] The polycrystalline nature of the films is further supported by the multiple reflection planes noted in all the samples. The thermally grown film ($t_c = 0$ s) displays crystallite growth relating to the (100), (002), (101), (110), and (103) reflections. Increasing $t_c$ induces preferential growth in

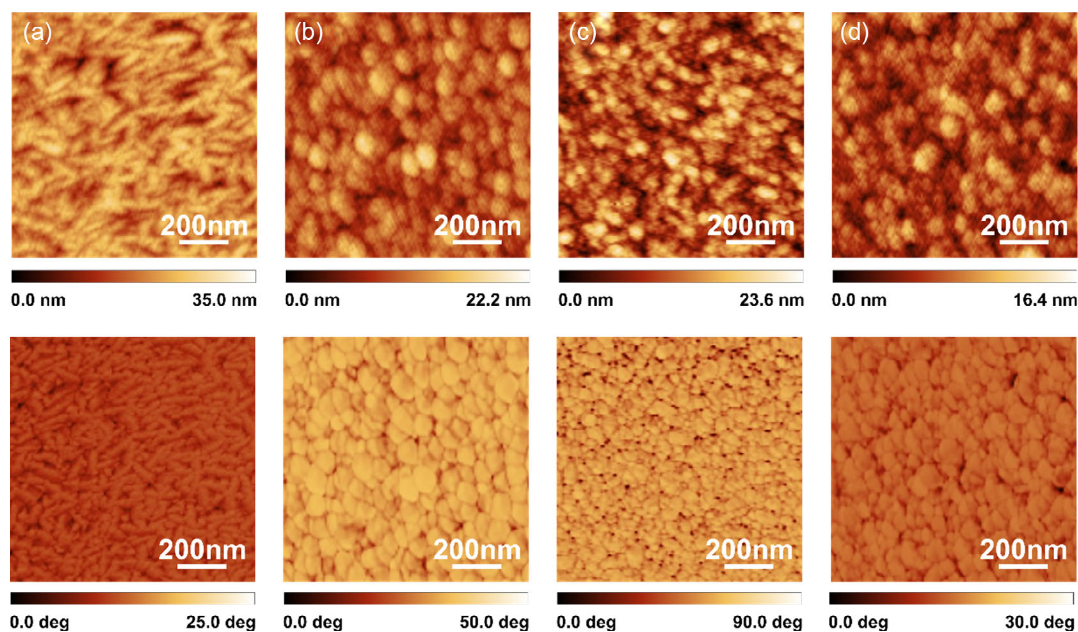


**Figure 3.** The topography (top) and phase contrast (bottom) AFM images of the AZO thin films deposited by ALD with in situ $O_2$ plasma treatment times ($t_c$) of a) 0 s, b) 2 s, c) 4 s, and d) 6 s.


© 2023 The Authors. Small Structures published by Wiley-VCH GmbH

26884062, 0, Downloaded from https://onlinelibrary.wiley.com/doi/10.1002/sstr.202300140 by Test, Wiley Online Library on [26/07/2023]. See the Terms and Conditions (https://onlinelibrary.wiley.com/terms-and-conditions) on Wiley Online Library for rules of use; OA articles are governed by the applicable Creative Commons License

26884062, 0, Downloaded from https://onlinelibrary.wiley.com/doi/10.1002/sstr.202300140 by Test, Wiley Online Library on [26/07/2023]. See the Terms and Conditions (https://onlinelibrary.wiley.com/terms-and-conditions) on Wiley Online Library for rules of use; OA articles are governed by the applicable Creative Commons License

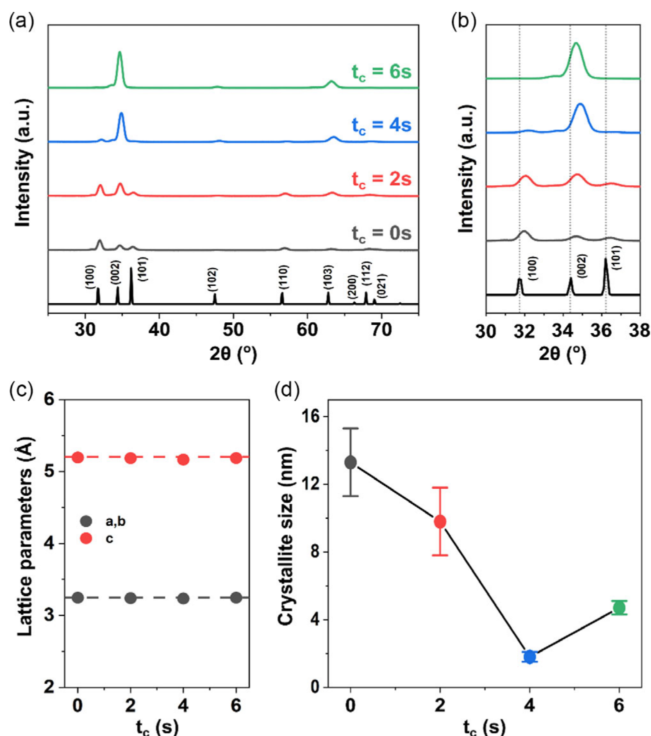


**Figure 4.** a) XRD patterns of the AZO thin films deposited by PE-ALD with a range of $O_2$ plasma treatment times. b) An enlarged view of the XRD spectra in the range of 30–38° to give insight into the observed peak shift. c) The refined lattice parameters as a function of in situ $O_2$ plasma treatment time ($t_c$). The dotted lines represent the lattice parameter values from ref. [51]. d) The derived crystallite sizes via the Williamson–Hall method as a function of in situ $O_2$ plasma treatment time ($t_c$).

the (002) plane. This is inferred from the increase in peak intensity of the (002) peak with increasing $t_c$. The claim of the formation of the nanopillars with longer in situ plasma treatment times ($t_c = 4$, 6 s) is supported by the significant suppression of all reflection planes excluding the (002) plane. This sort of behavior is of great interest for piezoelectric applications.[52]

It was also observed that there was a shift of the peak positions of the (100) and the (002) reflections to larger diffraction angles (Figure 4b).[26] This is due to the successful substitution of $Al^{3+}$ into $Zn^{2+}$ sites. This peak shift occurs due to the variation in the diameter of $Zn^{2+}$ (0.74 Å) and $Al^{3+}$ (0.53 Å).[26,49] It should be noted that the absence of peaks related to $Al_2O_3$ suggests successful doping of Al into the ZnO matrix and no $Al_2O_3$ grain formation which is detrimental to carrier concentration and mobility, leading to inferior electrical transport properties.[53]

All the AZO films refined lattice parameters consistent with reports in the literature ($a$, $b = 3.2498$ and $c = 5.2066$ Å), as shown in Figure 4c.[54] Crystallite sizes are presented in Figure 4d and were determined via the Williamson–Hall method.[55] Errors in crystallite size were estimated using the standard error of the linear regression used as part of the Williamson–Hall method. The thermally grown AZO film yielded a crystallite size of 13.3(2) nm. This was noted to significantly decrease with the introduction of an in situ $O_2$ plasma step, with crystallite sizes of 9.8(2), 1.8(0.3), and 4.7(0.4) nm for $O_2$ plasma treatment times $t_c = 2$, 4, and 6 s, respectively. This is consistent with the apparent grain size displayed in the SEM and AFM images shown in Figure 2 and 3 and supports the enhanced grain growth of the $t_c = 6$ s film. This modulation of grain morphology is similar to reports by Thomas and Cui on ZnO films deposited by PE-ALD.[56]

### 2.2. Ultralow Thermal Conductivity of PE-ALD-Deposited AZO Thin Films

The strong ionic nature of the bonds often exhibited in oxide-based materials leads to large thermal conductivities. ZnO is no exception, with the thermal conductivity of bulk ceramic ZnO being 50 $W\,m^{-1}\,K^{-1}$.[57] Nanostructured films have been shown to have reduced thermal conductivity with thin film ZnO being reduced to a few $W\,m^{-1}\,K^{-1}$.[58–60] Here, we investigated the thermal conductivity of AZO thin films using a custom-built $\omega-3\omega$ setup using the method presented by Cahill.[61,62] **Figure 5**a illustrates the schematic of the fabricated structure used for the $\omega-3\omega$ method to determine the thermal conductivity of our AZO films. Detailed information on the setup and method can be found in the Experimental Section and Section S1, Supporting Information.

Figure 5b shows the in-phase and out-of-phase third harmonic voltages ($V_{3\omega}$) at frequencies ranging from $10^2$ to $10^4$ Hz. Despite being able to derive the thermal conductivity directly from the out-of-phase component, the small magnitude makes this more prone to error and derivation from the in-phase contribution more accurate. With increasing frequency, it is apparent that $V_{3\omega}$ decreases, which suggests a similar relation to the temperature oscillation across the film. This stems from a reduction in the effective heating time at higher frequencies. Figure 5c shows the thermal conductivity of the AZO thin films deposited by PE-ALD. The $t_c = 0$ s film yielded a thermal conductivity of 1.12 $W\,m^{-1}\,K^{-1}$. The thermal conductivity of the plasma-treated films yielded significantly lower thermal conductivities of 0.68, 0.23, and 0.16 $W\,m^{-1}\,K^{-1}$ for $t_c = 2$, 4, and 6 s, respectively.

The significant reduction can be attributed to the significant reduction in grain size of the plasma-treated films. Work reported by Park et al showed a correlation between decreasing thermal conductivity with decreasing grain size.[58,59] The AZO nanopillars formed yielded outstandingly low thermal conductivities, which is the lowest thermal conductivities reported for Al-doped ZnO thin films in the literature. The reported values also appear to be lower than predictions of amorphous ZnO which is predicted to be ≈1.3 $W\,m^{-1}\,K^{-1}$.[63] This suggests the formation of nanopillar structures in our AZO films through $O_2$ plasma treatment is an effective way to enhance phonon interface scattering and depress thermal conductivity.[64] Similar behaviors were also observed in other reported works where the reduction can be achieved by superlattice structures.[64,65]

### 2.3. Improved Thermoelectric Properties of PE-ALD-Deposited AZO Thin Films

Variable temperature thermoelectrical measurements were conducted to investigate the temperature dependence of the AZO thin films. Errors were determined by taking the standard


© 2023 The Authors. Small Structures published by Wiley-VCH GmbH

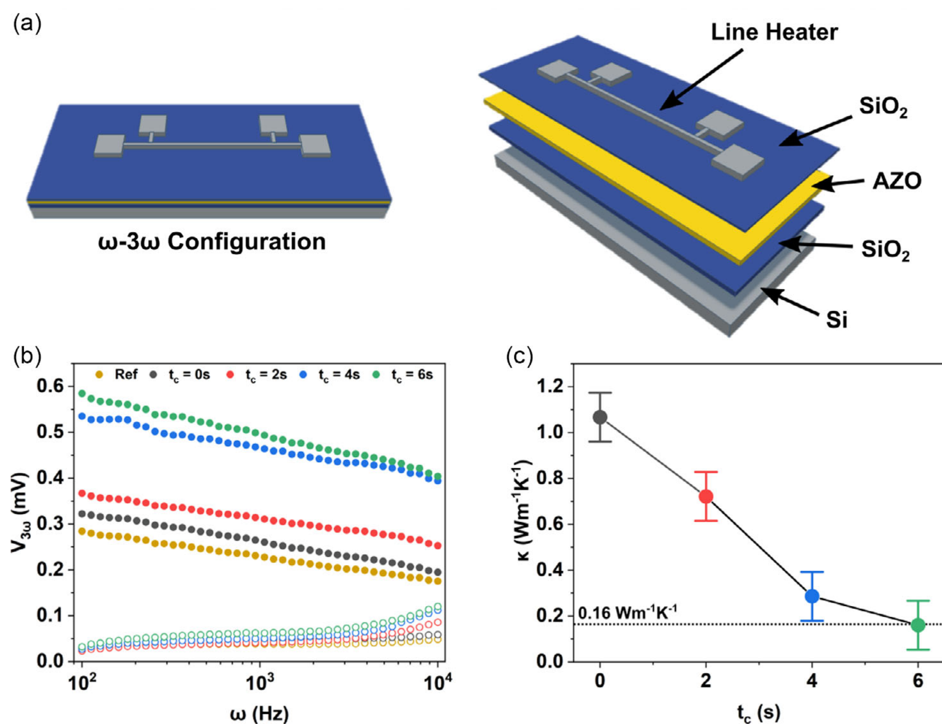


**Figure 5.** a) Schematic of the fabricated structure used for the $\omega$–$3\omega$ method to determine thermal conductivity. b) The in-phase (dots) and out-of-phase (circles) third harmonic voltages ($V_{3\omega}$); c) thermal conductivity of the various Al-doped ZnO thin films deposited by PE-ALD with varying in situ $O_2$ plasma times.

deviation of multiple measurements at each temperature. The electrical conductivity, as shown in **Figure 6**a, displayed weak temperature dependence over a wide temperature range. All films yielded electrical conductivities in the range of 200–700 S $cm^{-1}$. The electrical conductivity of the thermally grown AZO thin film was 559.4 S $cm^{-1}$ at room temperature. The $t_c = 2$ s film noted a reduction in electrical conductivity yielding a conductivity of 257.3 S $cm^{-1}$ at room temperature. However, with a further increase in $O_2$ plasma exposure to $t_c = 4$ and 6 s, the conductivity increases to 612.4 and 466.2 S $cm^{-1}$, respectively.

To investigate the mechanism governing the electrical conductivity at various temperatures, Hall measurements were taken with the carrier mobility shown in Figure 6b and carrier concentration in Figure 6c. It can be observed that variations in carrier mobility and carrier concentration are relatively small. At room temperature, the thermally grown AZO thin film has a moderate mobility of 16.4 $cm^2 V^{-1} s^{-1}$ and a high carrier concentration of $2.13 \times 10^{20}$ $cm^{-3}$, which is likely driven by the formation of hydrogen complexes which originate from the hydrogen present in the $H_2O$ precursor.[66–68] Such carrier concentration is significantly larger than the criteria of the degenerate ZnO semiconductor ($n > 3.7 \times 10^{18}$ $cm^{-3}$),[69] which is the main contributor to the weak temperature dependence of electrical conductivity observed from our films. Similar behaviors are reported on AZO thin films under similar temperature ranges.[20,37,70] It appears that the mobility of the plasma-treated films increased with longer exposure times, which is due to the enhancement of the (002) plane. The suppression of the $t_c = 2$ s film's carrier mobility is due to enhanced grain boundary scattering. The origin of this arises from variation in grain boundary orientation which is consistent with reports from Nomoto et al.[71] This is supported by the similar peak intensity observed in both the (100) and (002) reflections observed in Figure 4a. The preferential growth of the (002) plane observed in the $t_c = 4$ and 6 s films would result in the frequency of grain boundaries being reduced, thus resulting in higher carrier mobilities. Similar reports of preferential growth of (002) plane reducing resistivity have been found by Dasgupta et al.[72] The carrier concentrations of the plasma-treated films were all lower than the thermally grown film. This is likely due to the removal of the hydrogen complexes via the $O_2$ plasma treatment.[45,66–68] Figure 6d presents the Seebeck coefficient measurements for all the plasma-treated AZO films deposited by PE-ALD at variable temperatures. All films are n-type which agrees well with the Hall measurement results and literature.[49] It was found that all samples had an increase of S with temperature which is due to the broadening of the Fermi function. The untreated film ($t_c = 0$s) yielded the lowest Seebeck coefficient and was found to increase in the plasma-treated films.

The AZO thin films' variable temperature power factors are exhibited in **Figure 7**a with the $t_c = 4$ s film displaying the highest performance. A maximum power factor of 80 μW $m^{-1} K^{-2}$ is achieved at room temperature and 294 μ W$m^{-1} K^{-2}$ at 563 K. The room temperature figure-of-merit $ZT$ values for all films were calculated using Equation (1). Significant improvement of $ZT$ is achieved for AZO films with $O_2$ plasma treatments ($t_c = 4$ and 6 s) which achieved $ZT$ values of 0.11 and 0.09, respectively, which is a near-order higher when compared with the


© 2023 The Authors. Small Structures published by Wiley-VCH GmbH

26884062, 0, Downloaded from https://onlinelibrary.wiley.com/doi/10.1002/sstr.202300140 by Test, Wiley Online Library on [26/07/2023]. See the Terms and Conditions (https://onlinelibrary.wiley.com/terms-and-conditions) on Wiley Online Library for rules of use; OA articles are governed by the applicable Creative Commons License

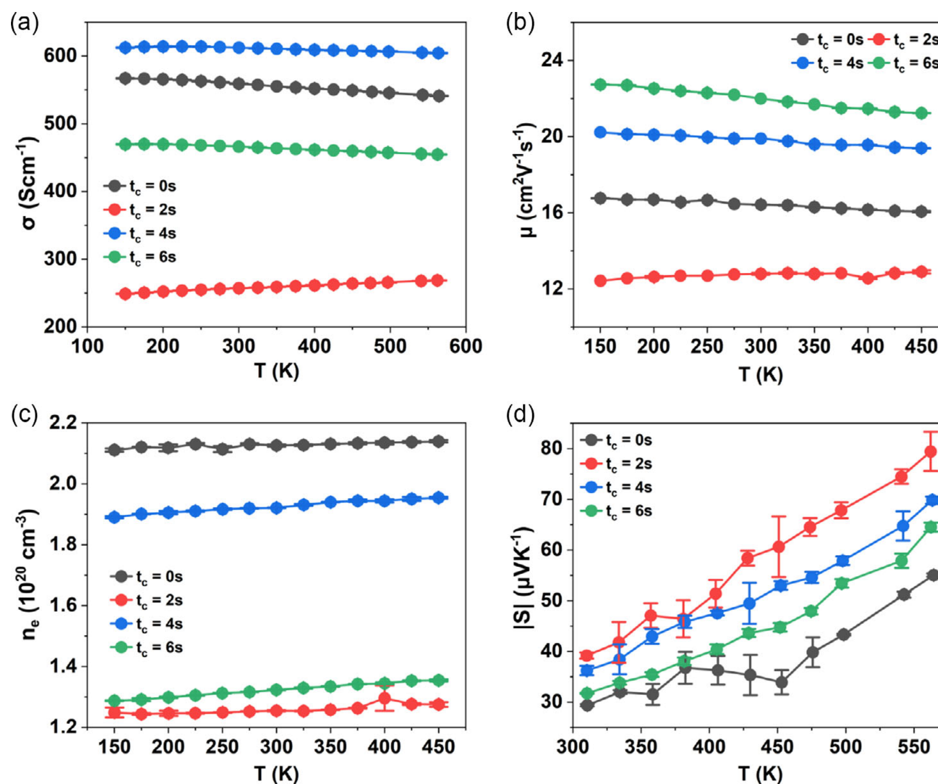


**Figure 6.** Variable temperature measurements of a) electrical conductivity ($\sigma$), b) carrier mobility ($\mu$), and c) carrier concentration ($n_e$). d) Variable temperature measurements of the absolute Seebeck coefficient ($S$) in the range of 300–575 K.

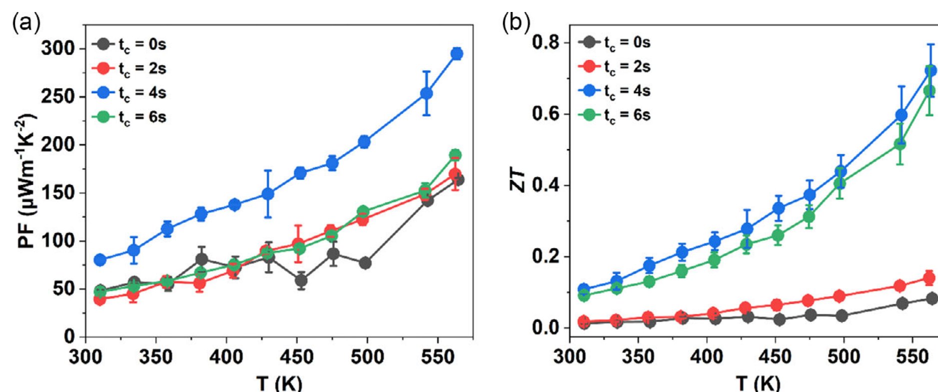


**Figure 7.** Variable temperature a) power factor (PF) and b) $ZT$ of the AZO thin films deposited by PE-ALD with varying $t_c$. $ZT$ values at variable temperatures are estimated under the assumption that thermal conductivity does not vary significantly over the temperature range.

untreated film ($t_c = 0$ s), with a $ZT \approx 0.01$. This improvement can be predominantly ascribed to the ultralow thermal conductivity of these two films.

The $ZT$ values at variable temperatures for all films (Figure 7b) are calculated under the assumption that the thermal conductivity is independent of the temperature. We believe this is a reasonable assumption considering 1) the relative independence of electrical conductivity against temperature for our AZO films, and 2) that the phonon contribution to the thermal conductivity normally decreases with increasing temperature. It is shown that our $t_c = 4$s film demonstrates a $ZT$ of 0.72 at 563 K. **Table 1** compares the thermoelectric properties of our AZO film with other reported works. To the best of our knowledge, our AZO film with in situ $O_2$ plasma treatment registers the highest value ever reported in ZnO-based thermoelectric thin films and shows great potential for its application in thermal energy harvesting.

### 2.4. Prototype of AZO Thin Film-Based Lateral μ-TEG

To gain an insight into the potential power generation capacity of our AZO thin films, a prototype single-leg lateral μ-TEG was


© 2023 The Authors. Small Structures published by Wiley-VCH GmbH

26884062, 0, Downloaded from https://onlinelibrary.wiley.com/doi/10.1002/sstr.202300140 by Test, Wiley Online Library on [26/07/2023]. See the Terms and Conditions (https://onlinelibrary.wiley.com/terms-and-conditions) on Wiley Online Library for rules of use; OA articles are governed by the applicable Creative Commons License

26884062, 0, Downloaded from https://onlinelibrary.wiley.com/doi/10.1002/sstr.202300140 by Test, Wiley Online Library on [26/07/2023]. See the Terms and Conditions (https://onlinelibrary.wiley.com/terms-and-conditions) on Wiley Online Library for rules of use; OA articles are governed by the applicable Creative Commons License

**Table 1.** Thermoelectric properties of the ZnO-based thin films reported in the literature compared to our highest performing AZO film ($t_c = 4$ s).

| Deposition method | Composition | $T_{Max}$ [K] | $\sigma$ [S cm$^{-1}$] (300 K/$T_{Max}$) | $\|S\|$ [μV K$^{-1}$] (300 K/$T_{Max}$) | $\kappa$ [W m$^{-1}$ K$^{-1}$] (300 K/$T_{Max}$) | PF [μ Wm$^{-1}$ K$^{-2}$] (300 K/$T_{Max}$) | $ZT$ (300 K/$T_{Max}$) | References |
|---|---|---|---|---|---|---|---|---|
| This work | Al:ZnO | 563 | 612.4/604.5 | 36.2/69.8 | 0.23/– | 80/294 | 0.110/0.720 | |
| ALD | Al:ZnO | – | 279/– | 107/– | –/– | 319/– | –/– | [80] |
| ALD | Al:ZnO | 473.15 | 980/1196 | 59/72 | –/– | 340/620 | –/– | [81] |
| ALD | Al:ZnO (SL) | – | 107/– | 62/– | 1.04/– | 42/– | 0.014/– | [82] |
| ALD | (Al, HQ):ZnO (SL) | – | 14/– | 60/– | 3.56/– | 5/– | –/– | [83] |
| ALD | ZnO | 453.15 | 92/80 | 110/140 | 3.80/– | 111/155 | 0.009/– | [84] |
| ALD | Zr:ZnO | 453.15 | 139/66 | 92/138 | 3.07/– | 117/122 | 0.011/– | [84] |
| Sputtering | ZnO | 383.15 | 42/53 | 88/97 | 4.60/4.70 | 33/50 | 0.003/0.004 | [85] |
| Sputtering | (Ga, In):ZnO | 383.15 | 1095/1078 | 23 /29 | 2.00/1.80 | 58/89 | 0.009/0.019 | [85] |
| Sputtering | (Ga, In):ZnO (SL) | 480 | 23/21 | 170/195 | 1.46/– | 67/80 | –/– | [86] |
| Sputtering | Al:ZnO | – | 153/– | 45/– | –/– | 31/– | –/– | [87] |
| Sputtering | (Al, In):ZnO | – | 95/– | 153/– | –/– | 222/– | –/– | [87] |
| Sputtering | Al:ZnO | – | 2045/– | 21/– | –/– | 90/– | –/– | [35] |
| Sputtering | Al:ZnO | 350 | 476/479 | 38/39 | –/– | 70/73 | –/– | [88] |
| Sputtering | Sb:ZnO | 773 | 90/140 | 107/170 | –/– | 103/406 | –/– | [89] |
| Sputtering | (Ga, In):ZnO | 573 | 1700/1521 | 22/70 | 2.4/2.2 | 82/745 | 0.010/0.200 | [90] |
| MCVD | Al:ZnO | 600 | 54/57 | 108/163 | 5.54/– | 63/152 | 0.003/0.016 | [37] |
| MCVD | Al:ZnO | 600 | 10/13 | 166/212 | 0.60/– | 26/57 | 0.014/0.057 | [37] |
| MBVD | Al:ZnO | 513.15 | –/546 | –/29.5 | –/– | –/48 | –/– | [91] |
| PLD | Al:ZnO | 600 | 74/93 | 119/203 | 4.89/4.89 | 105/383 | 0.006/0.045 | [92] |
| PLD | Al:ZnO | | 310/382 | 65/121 | –/– | 131/559 | –/– | [93] |
| PLD | (Ga, Ni, Al):ZnO | 673 | 767/494 | 35/80 | –/– | 92/313 | –/– | [27] |
| PLD | Ga:ZnO | 623 | 1000/1034 | 36/65 | –/– | 126/439 | –/– | [94] |
| Sol-gel | Al:ZnO | | –/– | –/– | 1.10/– | –/– | –/– | [38] |
| Spray pyrolysis | Al:ZnO | 390 | –/– | 100/150 | –/– | –/– | –/– | [95] |
| Thermal evaporation | (CNT, Al):ZnO | 570 | 88/39 | 115/165 | 2.20/1.16 | 115/106 | 0.016/0.052 | [96] |
| Thermal evaporation | Al:ZnO | 560 | 133/169 | 152/193 | –/– | 307/627 | –/– | [59] |
| Vacuum evaporation | Al:ZnO | 819 | 830/192 | 53/120 | 0.9 | 233/274 | 0.078/– | [43] |

fabricated, as shown in **Figure 8**a. The μ-TEG was fabricated on $Si/SiO_2$ substrate using the optimized AZO film ($t_c = 4$s) as the n-leg and Al metal as the p-leg and the interconnects. The outer terminals of the μ-TEG are connected to a load resistor of which a parametric sweep is applied from $10^2$ to $10^6\,\Omega$ to resistance match for maximum power output. A 2nd order polynomial is used to fit the $I$–$P$ curve with a differential being taken to determine maximum power output. During the electrical measurements, infrared images (shown in Figure 8b) were taken concurrently to reveal the real-time temperature profile across the μ-TEG. These profiles were also fed into a finite-element-method-based simulation of the same TEG using COMSOL Multiphysics.[73] More information about the fabrication and simulation can be found in the Experimental Section and Section S2, Supporting Information.

Figure 8c,d displays the experimental (circles) $I$–$V$ and $I$–$P$ curves for the AZO-based μ-TEG at different temperature conditions. It can be observed that these results are well matched (within 5% accuracy) to the COMSOL simulation results (shaded) under the same conditions. Figure 8e presents the open-circuit voltages against temperature differences. It is not surprising that a linear relationship between the voltage and temperature difference is observed. The effective Seebeck value for each thermocouple is derived to be $-35.6\ \mu V\ K^{-1}$, which agrees well with the Seebeck data collected in Figure 6d. Figure 8f presents the device's maximum power output against $\Delta T$ where a maximum power of 1.08 nW is obtained. This is competitive with reports of oxide-based generators, which are summarized in **Table 2**.

It should be noted that the outstanding thermoelectric properties, especially the ultralow thermal conductivity, achieved in this work were not reflected in the device performance. This is due to the fact that the thermal conductance of the lateral μ-TEG in this work is dominated by the Si substrate which is significantly thicker (≈675 μm) than the AZO layer. The high thermal conductivity of Si (≈100 W m$^{-1}$ K) leads to a high device thermal conductance which limits the performance of the device. However, it is worth mentioning that μ-TEG demonstrated in this work is a proof-of-concept prototype and has great potential for improvements through device scaling (Figure S8, Supporting


© 2023 The Authors. Small Structures published by Wiley-VCH GmbH

26884062, 0, Downloaded from https://onlinelibrary.wiley.com/doi/10.1002/sstr.202300140 by Test, Wiley Online Library on [26/07/2023]. See the Terms and Conditions (https://onlinelibrary.wiley.com/terms-and-conditions) on Wiley Online Library for rules of use; OA articles are governed by the applicable Creative Commons License

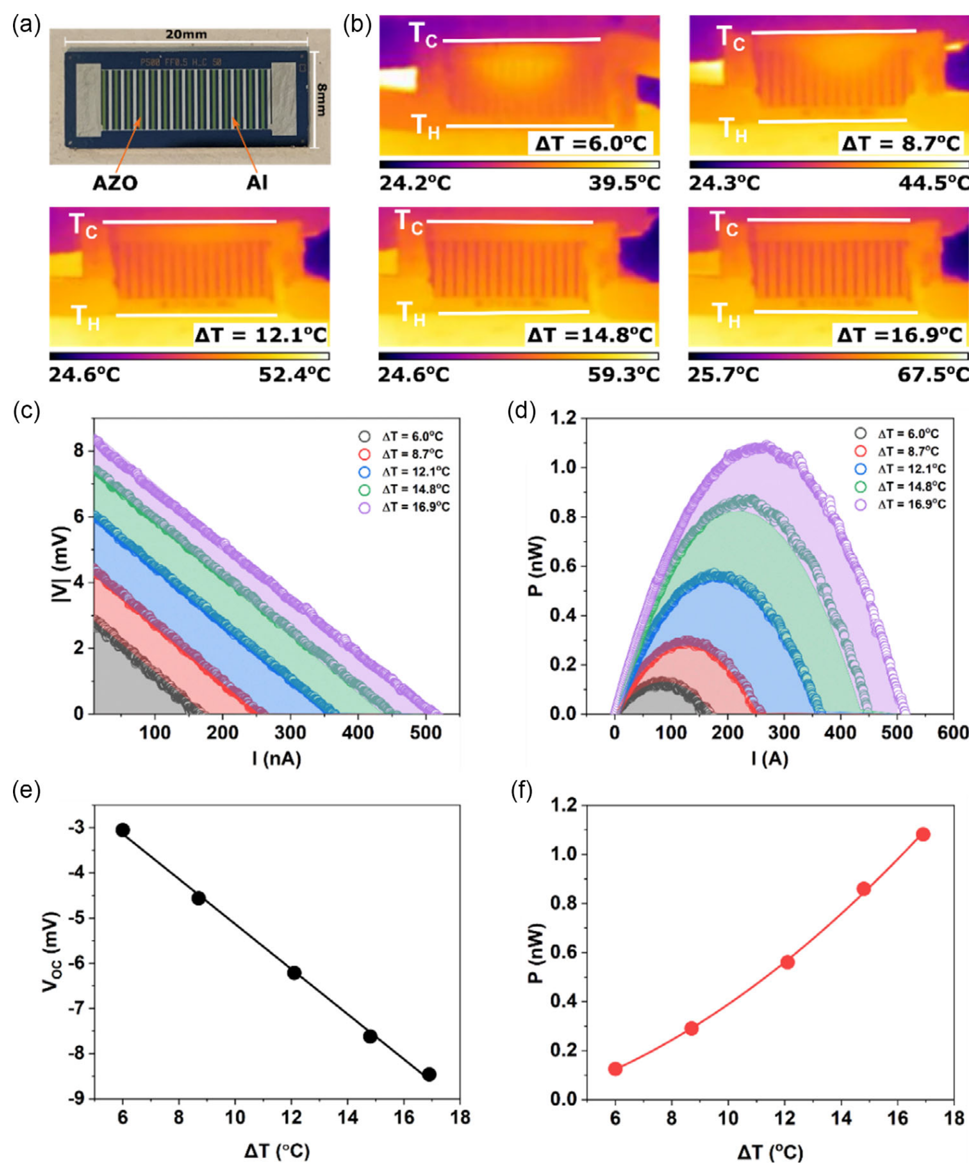


**Figure 8.** a) Optical image of the fabricated lateral TEG. b) IR images to indicate the temperature difference applied across the fabricated device. Simulated (shaded) and experimental (circles) c) *I–V* and d) *I–P* curves for our fabricated thin-film TEG. e) The open-circuit voltage and f) power output against the temperature difference ($\Delta T$).

Information) and other approaches. For example, further optimization of carrier concentration can be pursued to maximize the thermoelectric performance of the AZO thin films; integration of full μ-TEG with both n- and p-legs could also lead to higher power generation; implementing the AZO film into different μ-TEG architectures such as flexible substrates with high thermal resistance can improve its energy efficiency and further widen its application scenarios.

## 3. Conclusions

In summary, we reported the improved thermoelectric performance of AZO thin films via a PE-ALD process using an in situ $O_2$ plasma treatment. The $O_2$ plasma treatment facilitates the growth of a dense array of AZO nanopillars perpendicular to the substrate while promoting Al doping in the film. This has led to the modulation of AZO electrical properties where a maximum electrical conductivity of 612.4 S cm$^{-1}$ is achieved with a 4 s plasma exposure. Variable temperature thermoelectric performance of our AZO films was reported across a wide temperature range, of which an encouraging power factor of 294 μW m$^{-1}$ K$^{-2}$ at 563 K was achieved. Thermal conductivity measurements were also conducted, with the lowest thermal conductivity of 0.16 W m$^{-1}$ K$^{-1}$, which is, to the best of our knowledge, the lowest reported thermal conductivity for AZO thin films. This has resulted in the highest $ZT$ value of 0.72 that has ever been reported in ZnO-based thermoelectric thin films. In addition,


© 2023 The Authors. Small Structures published by Wiley-VCH GmbH

26884062, 0, Downloaded from https://onlinelibrary.wiley.com/doi/10.1002/sstr.202300140 by Test, Wiley Online Library on [26/07/2023]. See the Terms and Conditions (https://onlinelibrary.wiley.com/terms-and-conditions) on Wiley Online Library for rules of use; OA articles are governed by the applicable Creative Commons License

**Table 2.** Current literature on oxide-based μ-TEGs reported in literature using a range of different deposition methods. The number of thermocouples used for the devices is stated along with the applied temperature difference and the subsequent output power ($P_{out}$) and density. SL represents superlattice structure.

| Material | Deposition method | #TC | $\Delta T$ [°C] | $P_{out}$ [nW] | References |
|---|---|---|---|---|---|
| n-AZO | ALD | 14 | 16.9 | 1.08 | Our work |
| p-Al | | | | | |
| n-CuO | Thermal evaporation | 5 | | | [97] |
| p-ZnO | | | | | |
| n-ZnO | PLD | 4 | 160 | 1.8 | [98] |
| p-$SnO_x$ | | | | | |
| n-$Al_2O_3$–ZnO SL | ALD | 4 | 80 | 1.01 | [82] |
| p-$Bi_{0.5}Sb_{1.5}Te_3$ | | | | | |
| n-ZnO:In | SILAR | 8 | 50 | ≈ 0.65 | [99] |
| p-Al | | | | | |

our AZO film was integrated into a proof-of-concept prototype device and achieved an encouraging peak power output of 1.08 nW at a temperature difference of 16.9 °C with great potential for further improvement. This work points toward the potential application of AZO-based TEGs as a novel and sustainable power solution for IoT applications.

## 4. Experimental Section

*Deposition of Al-Doped ZnO via ALD*: The Al-doped ZnO thin films were deposited on $Si/SiO_2$ substrates via ALD using an OIPT FlexAl ALD system equipped with DEZ, TMA, and $H_2O$ as precursors. All depositions were conducted at 175 °C with argon as a purging gas. Before each deposition, a 10 min prepurge was conducted to clean the chamber. An initial 16 DEZ cycles were also conducted; this along with the initial plasma step would improve film adhesion. A target Al/Zn cycle ratio of 4% was chosen similarly to previous work,[41] which is below the solubility limit of Al in the ZnO matrix.[74,75]

The supercycle of the ALD process, as shown in Figure 1, begins with the introduction of DEZ vapor with a pulse length of $t_1 = 0.125$ s. For the DEZ cycle, the chamber pressure was set at 150 mTorr. This was then subsequently followed by a purge step ($t_p = 5$ s) and then the introduction of $H_2O$ vapor with a dose time of 0.150 s ($t_3 = 0.150$ s). For the DEZ cycle, the Ar gas had a flow rate of 250 sscm. Each DEZ cycle was followed by an in situ $O_2$ plasma step in which the exposure length was varied ($t_c = 0$, 2, 4, 6 s). The chamber pressure was reduced to 15 mTorr for the $O_2$ plasma step. This was then followed by the introduction of the Al dopant in the form of a TMA cycle. The TMA cycle consists of TMA vapor being introduced with a pulse length ($t_2 = 0.020$ s) and was conducted with the chamber pressure set at 80 mTorr. This was similarly followed by a purge step and the introduction of water vapor as a reactant. The Ar flow rate for the TMA cycle was 100 sscm. For each 24 DEZ cycles, one cycle of TMA was introduced to aim for a target Al/Zn composition of ≈4%. This supercycle was repeated to reach a target thickness of ≈200 nm. All films were subject to a 30 min anneal at 400 °C using the Jipelec Jetfirst 200 Rapid thermal annealing system.

*AZO Thin Film Characterization*: The AZO films deposited by ALD were characterized using a combination of technical tools. The morphology was investigated by SEM using the Jeol JSM 7500F FESEM with an accelerating voltage of 5 kV. Film thicknesses were confirmed via ellipsometry (VASE, J.A. Woollam Co. M-2000) fitted with the Drude model and cross-sectional SEM imaging. The AFM measurements were taken using the XE7 system from Park System. The high resonance frequency cantilever probes with a tip diameter of 10 nm were used to measure the surface roughness. The topography and phase signals of the sample surface were measured by using tapping mode. The resolution of the images was 256 × 256 pixels, and the scanning speed was 0.5 Hz and the scanning area is of 1 × 1 μm$^2$. For samples, the values of surface roughness and phase contrast were processed by AFM software Gwyddion. XRD patterns were collected in grazing incidence mode ($\theta_1 = 1°$) using a Rigaku SmartLab diffractometer (Cu Kα, $\lambda = 1.5418$ Å) with parallel X-ray beam and a Hypixdetector operated in 1D mode. Phase matching and lattice parameter calculations were undertaken using the PDXL2 software package[76] and diffraction patterns from ICSD.[77]

Electrical characterization was conducted using a Nanometrics HL5500 Hall effects system with a Van der Pauw configuration. This system has cryogenic capability allowing measurements of electrical conductivity in a temperature range of 150–450 K. Electrical conductivity ($\sigma$) measurements were conducted in situ with Hall measurements determining carrier mobility ($\mu$) and carrier density ($n$) under a magnetic field of 0.5 T. Probes were ensured to be appropriately in contact with samples before each measurement. *I–V* curves were recorded before each measurement to ensure Ohmic conduction as well as to optimize current for maximized voltage signal (20 mV). Variable temperature thermoelectric properties were measured using a JouleYacht thin-film thermoelectric parameter test system (MRS-3L) with the system calibrated using a nickel foil reference standard. During the temperature dependent measurement, the sample is clamped on the testing stage in the vacuum chamber. The stage will be heated to the target temperatures for measurements. Once the target temperature is reached and stabilized, the measurement will begin. For each Seebeck measurement, one side of the sample will be heated up to create small temperature differences (0–10 K) across the sample while the generated voltages are measured concurrently. After each measurement, the Seebeck coefficient at this target temperature can be calculated through a linear fit of the voltage–temperature difference relation. Subsequently, the stage is heated to the next target temperature for the next measurement. This system allows further extension of the electrical conductivity measurement range to ≈550 K as well as simultaneous measurements of thermopower.

Thermal conductivity was conducted using a custom-built $\omega$–3$\omega$ method setup. The detailed process is presented in Section S1, Supporting Information. Samples were prepared as shown in Figure 5a. An AZO layer (≈200 nm) is deposited via ALD on a $Si/SiO_2$ substrate with a 300 nm $SiO_2$ film as an insulation layer. After AZO deposition, a 200 nm $SiO_2$ layer was sputtered to act as electrical insulation to isolate the AZO film to the line heater/sensor. It is worth mentioning that $\omega$–3$\omega$ measurement for thin film thermal conductivity is known to be challenging and always comes with factors (e.g., parasitic heat losses, nonideal distribution of current and temperature) that can cause uncertainty in the measured values, leading to a system error of 5–10% which is included in our measured results.[78,79]

Optical lithography using AZ nLof 2070 negative photoresist followed by sputtered Al (≈200 nm) was conducted to fabricate the line heater pattern as shown in Figure S1, Supporting Information. As this technique is a differential method, a reference sample without the AZO film is also fabricated. The line heater is connected into a Wheatstone bridge configuration to eliminate the large first harmonic voltage and is wired to the SR850 lock-in to extract the third harmonic voltage ($V_{3\omega}$). Samples were loaded into a temperature-controlled Instec HCP421V-PM probe station using high-temperature vacuum grease to improve thermal contact. The stage is held under vacuum and then heated to ≈65 °C at a rate of 10 °C min$^{-1}$ to allow sufficient time for the sample temperature to stabilize. Input current is supplied by the DS360 function generator and is measured using the Agilent DSO6012A oscilloscope. Resistance measurements were taken using the Fluke 8088A digital multimeter at increments of 2.5 °C in the range of ≈25 to ≈65 °C.

*Fabrication and Testing of Lateral AZO-Based μ-TEG*: To investigate the power generation performance of our plasma-treated films, a lateral thermoelectric generator was fabricated using the highest-performing AZO thin film ($t_c = 4$ s) as the n-leg and Al as p-leg and the interconnect material. The fabrication process is shown in Figure S5, Supporting


© 2023 The Authors. Small Structures published by Wiley-VCH GmbH

Information, with detailed fabrication and testing information presented in Section S2, Supporting Information.

## Supporting Information

Supporting Information is available from the Wiley Online Library or from the author.

## Acknowledgements

The authors thank the ADEPT project funded by a Programme Grant from the EPSRC (EP/N035437/1). V.S. would like to thank the EPSRC DTP studentship (EP/R513325/1). The authors also gratefully acknowledge funding for thin film diffraction and NMR instrumentation from the EPSRC through EP/K00509X, EP/K009877/1, and EP/K039466/1. All data supporting this study are openly available from the University of Southampton repository at DOI: https://doi.org/10.5258/SOTON/D2674.

## Conflict of Interest

The authors declare no conflict of interest.

## Data Availability Statement

The data that support the findings of this study are openly available in the University of Southampton's repository at https://doi.org/10.5258/SOTON/D2674, reference number 2647.

## Keywords

aluminum-doped zinc oxide (AZO), micro-thermoelectric generators, $O_2$ plasma treatment, thermal conductivity, thermoelectrics

Received: April 21, 2023
Revised: June 27, 2023
Published online:

[1] T. Sanislav, G. D. Mois, S. Zeadally, S. C. Folea, *IEEE Access* **2021**, *9*, 39530.
[2] M. Haras, T. Skotnicki, *Nano Energy* **2018**, *54*, 461.
[3] W. Y. Chen, X. L. Shi, J. Zou, Z. G. Chen, *Mater. Sci. Eng. R: Rep.* **2022**, *151*, 100700.
[4] B. Hu, X. L. Shi, J. Zou, Z. G. Chen, *Chem. Eng. J.* **2022**, *437*, 135268.
[5] Z. H. Zheng, X. L. Shi, D. W. Ao, W. Di Liu, M. Li, L. Z. Kou, Y. X. Chen, F. Li, M. Wei, G. X. Liang, P. Fan, G. Q. M. Lu, Z. G. Chen, *Nat. Sustainability* **2022**, *6*, 180.
[6] Z. Yuan, X. Tang, Y. Liu, Z. Xu, K. Liu, J. Li, Z. Zhang, H. Wang, *J. Power Sources* **2019**, *414*, 509.
[7] A. Amin, R. Huang, D. Newbrook, V. Sethi, S. Yong, S. Beeby, I. Nandhakumar, *J. Phys. Energy* **2022**, *4*, 024003.
[8] K. A. Morgan, I. Zeimpekis, Z. Feng, D. Hewak, *Thin Solid Films* **2022**, *741*, 139015.
[9] F. Tohidi, S. Ghazanfari Holagh, A. Chitsaz, *Appl. Therm. Eng.* **2022**, *201*, 117793.
[10] C. Gayner, K. K. Kar, *Prog. Mater. Sci.* **2016**, *83*, 330.
[11] Y. Wu, P. Nan, Z. Chen, Z. Zeng, R. Liu, H. Dong, L. Xie, Y. Xiao, Z. Chen, H. Gu, W. Li, Y. Chen, B. Ge, Y. Pei, *Adv. Sci.* **2020**, *7*, 1902628.
[12] F. Robinson, V. Sethi, C. H. K. De Groot, A. L. Hector, R. Huang, G. Reid, *ACS Appl. Mater. Interfaces* **2021**, *13*, 47773.
[13] X.-L. Shi, W.-D. Liu, M. Li, Q. Sun, S.-D. Xu, D. Du, J. Zou, Z.-G. Chen, X.-L. Shi, Z.-G. Chen, W.-D. Liu, M. Li, S.-D. Xu, D. Du, J. Zou, Q. Sun, *Adv. Energy Mater.* **2022**, *12*, 2200670.
[14] X. Shi, J. Yang, J. R. Salvador, M. Chi, J. Y. Cho, H. Wang, S. Bai, J. Yang, W. Zhang, L. Chen, *J. Am. Chem. Soc.* **2011**, *133*, 7837.
[15] S. Chen, K. C. Lukas, W. Liu, C. P. Opeil, G. Chen, Z. Ren, *Adv. Energy Mater.* **2013**, *3*, 1210.
[16] B. Yu, M. Zebarjadi, H. Wang, K. Lukas, H. Wang, D. Wang, C. Opeil, M. Dresselhaus, G. Chen, Z. Ren, *Nano Lett.* **2012**, *12*, 2077.
[17] X. Liu, X. L. Shi, L. Zhang, W. Di Liu, Y. Yang, Z. G. Chen, *J. Mater. Sci. Technol.* **2023**, *132*, 81.
[18] D. R. Lide, *Metal and Oxide Densities Based CRC Handbook of Chemistry and Physics*, 85th ed., CRC Press, Boca Raton **2004**.
[19] O. Caballero-Calero, J. R. Ares, M. Martín-González, *Adv. Sustainable Syst.* **2021**, *5*, 2100095.
[20] S. Saini, P. Mele, H. Honda, K. Matsumoto, K. Miyazaki, A. Ichinose, *J. Electron. Mater.* **2014**, *43*, 2145.
[21] B. Paul, E. M. Björk, A. Kumar, J. Lu, P. Eklund, *ACS Appl. Energy Mater.* **2018**, *1*, 2261.
[22] E. Ekström, A. le Febvrier, D. Fournier, J. Lu, V. L. Ene, N. Van Nong, F. Eriksson, P. Eklund, B. Paul, *J. Mater. Sci.* **2019**, *54*, 8482.
[23] A. Bhogra, A. Masarrat, R. Meena, D. Hasina, M. Bala, C. L. Dong, C. L. Chen, T. Som, A. Kumar, A. Kandasami, *Sci. Rep.* **2019**, *9*, article no. 14486.
[24] G. Korotcenkov, V. Brinzari, M. H. Ham, *Crystals* **2018**, *8*, 14.
[25] B. Luo, L. Cao, F. Luo, H. Zhou, K. Ma, D. Liu, L. Wang, S. Hu, K. Sun, S. Zhang, *Ceram. Int.* **2022**, *48*, 26188.
[26] Y. Wu, F. Cao, X. Ji, *J. Mater. Sci.: Mater. Electron.* **2020**, *31*, 17365.
[27] Z. Zhou, Y. Zheng, Y. Yang, W. Zhang, M. Zou, C. W. Nan, Y. H. Lin, *Crystals* **2022**, *12*, 1351.
[28] Y. H. Lin, J. Lan, C. Nan, *Oxide Thermoelectric Materials: From Basic Principles to Applications*, Wiley, Hoboken, NJ **2019.**
[29] M. Ohtaki, T. Tsubota, K. Eguchi, H. Arai, *J. Appl. Phys.* **1996**, *79*, 1816.
[30] T. Tsubota, M. Ohtaki, K. Eguchi, H. Arai, *J. Mater. Chem.* **1997**, *7*, 85.
[31] L. D. Hicks, M. S. Dresselhaus, *Phys. Rev. B* **1993**, *47*, 16631.
[32] L. D. Hicks, M. S. Dresselhaus, *Phys. Rev. B* **1993**, *47*, 12727.
[33] J. Mao, Z. Liu, Z. Ren, *npj Quantum Mater.* **2016**, *1*, article no. 16028.
[34] R. Venkatasubramanian, E. Siivola, T. Colpitts, B. O'Quinn, *Nature* **2001**, *413*, 597.
[35] L. Wen, M. Kumar, H. J. Cho, K. Leksakul, J. G. Han, *J. Phys. D: Appl. Phys.* **2017**, *50*, 185206.
[36] S. Saini, P. Mele, H. Honda, D. J. Henry, P. E. Hopkins, L. Molina-Luna, K. Matsumoto, K. Miyazaki, A. Ichinose, *Jpn. J. Appl. Phys.* **2014**, *53*, 060306.
[37] S. Saini, P. Mele, T. Oyake, J. Shiomi, J. P. Niemelä, M. Karppinen, K. Miyazaki, C. Li, T. Kawaharamura, A. Ichinose, L. Molina-Luna, *Thin Solid Films* **2019**, *685*, 180.
[38] T. H. Park, N. W. Park, J. Kim, W. Y. Lee, J. H. Koh, S. K. Lee, T.-H. Park, *J. Alloys Compd.* **2015**, *638*, 83.
[39] R. W. Johnson, A. Hultqvist, S. F. Bent, *Mater. Today* **2014**, *17*, 236.
[40] B. Swatowska, W. Powroźnik, H. Czternastek, G. Lewińska, T. Stapiński, R. Pietruszka, B. S. Witkowski, M. Godlewski, *Energies* **2021**, *14*, 6271.
[41] K. Sun, W. Xiao, S. Ye, N. Kalfagiannis, K. S. Kiang, C. H. de Groot, O. L. Muskens, *Adv. Mater.* **2020**, *32*, 2001534.
[42] H. Kim, in *Thin Solid Films*, Elsevier, Netherlands **2011**, pp. 6639–6644.
[43] S. Liu, G. Li, M. Lan, M. Zhu, K. Miyazaki, Q. Wang, *Ceram. Int.* **2021**, *47*, 17760.
[44] G. B. Lee, S. H. Song, M. W. Lee, Y. J. Kim, B. H. Choi, *Appl. Surf. Sci.* **2021**, *535*, 147731.


© 2023 The Authors. Small Structures published by Wiley-VCH GmbH

26884062, 0, Downloaded from https://onlinelibrary.wiley.com/doi/10.1002/sstr.202300140 by Test, Wiley Online Library on [26/07/2023]. See the Terms and Conditions (https://onlinelibrary.wiley.com/terms-and-conditions) on Wiley Online Library for rules of use; OA articles are governed by the applicable Creative Commons License

[45] R. Huang, S. Ye, K. Sun, K. S. Kiang, C. H. K. de Groot, *Nanoscale Res. Lett.* **2017**, *12*, 541.
[46] A. Seweryn, R. Pietruszka, B. S. Witkowski, A. Wierzbicka, R. Jakiela, P. Sybilski, M. Godlewski, *Crystals* **2019**, *9*, 554.
[47] Z. Baji, Z. Lábadi, Z. E. Horváth, G. Molnár, J. Volk, I. Bársony, P. Barna, *Cryst. Growth Des.* **2012**, *12*, 5615.
[48] G. K. H. Pang, K. Z. Baba-Kishi, A. Patel, *Ultramicroscopy* **2000**, *81*, 35.
[49] C. H. Zhai, R. J. Zhang, X. Chen, Y. X. Zheng, S. Y. Wang, J. Liu, N. Dai, L. Y. Chen, *Nanoscale Res. Lett.* **2016**, *11*, article no. 407.
[50] Z. Gao, P. Banerjee, *J. Vac. Sci. Technol., A* **2019**, *37*, 050802.
[51] A. Šarić, M. Vrankić, D. Lützenkirchen-Hecht, I. Despotović, Ž. Petrović, G. Dražić, F. Eckelt, *Inorg. Chem.* **2022**, *61*, 2962.
[52] R. Serhane, S. Abdelli-Messaci, S. Lafane, H. Khales, W. Aouimeur, A. Hassein-Bey, T. Boutkedjirt, *Appl. Surf. Sci.* **2014**, *288*, 572.
[53] Y. Wu, A. D. Giddings, M. A. Verheijen, B. Macco, T. J. Prosa, D. J. Larson, F. Roozeboom, W. M. M. Kessels, *Chem. Mater.* **2018**, *30*, 1209.
[54] L. Znaidi, T. Touam, D. Vrel, N. Souded, S. Ben Yahia, O. Brinza, A. Fischer, A. Boudrioua, *Coatings* **2013**, *3*, 126.
[55] B. Himabindu, N. S. M. P. Latha Devi, B. Rajini Kanth, *Mater. Today Proc.* **2021**, *47*, 4891.
[56] M. A. Thomas, J. B. Cui, *ACS Appl. Mater. Interfaces* **2012**, *4*, 3122.
[57] X. Wu, J. Lee, V. Varshney, J. L. Wohlwend, A. K. Roy, T. Luo, *Sci. Rep.* **2016**, *6*, article no. 22504.
[58] S. Saini, P. Mele, H. Honda, T. Suzuki, K. Matsumoto, K. Miyazaki, A. Ichinose, L. Molina Luna, R. Carlini, A. Tiwari, *Thin Solid Films* **2016**, *605*, 289.
[59] S. Liu, Y. Piao, G. Li, M. Lan, Y. Yuan, Q. Wang, *J. Appl. Phys.* **2020**, *127*, 055301.
[60] A. Kaźmierczak-Bałata, J. Bodzenta, M. Guziewicz, *Ultramicroscopy* **2020**, *210*, 112923.
[61] D. G. Cahill, *Rev. Sci. Instrum.* **1990**, *61*, 802.
[62] D. G. Cahill, R. O. Pohl, *Phys. Rev. B* **1987**, *35*, 4067.
[63] A. Roy, Y. T. Cheng, M. L. Falk, *J. Phys. Chem. C* **2016**, *120*, 2529.
[64] W. Y. Lee, J. H. Lee, J. Y. Ahn, T. H. Park, N. W. Park, G. S. Kim, J. S. Park, S. K. Lee, *Nanotechnology* **2017**, *28*, 105401.
[65] H. Mizuno, S. Mossa, J.-L. Barrat, *Sci. Rep.* **2015**, *5*, article no. 14116.
[66] B. K. Meyer, H. Alves, D. M. Hofmann, W. Kriegseis, D. Forster, F. Bertram, J. Christen, A. Hoffmann, M. Straßburg, M. Dworzak, U. Haboeck, A. V. Rodina, *Phys. Status Solidi B* **2004**, *241*, 231.
[67] C. G. Van De Walle, *Phys. Rev. Lett.* **2000**, *85*, 1012.
[68] T. A. Krajewski, K. Dybko, G. Luka, E. Guziewicz, P. Nowakowski, B. S. Witkowski, R. Jakiela, L. Wachnicki, A. Kaminska, A. Suchocki, M. Godlewski, *Acta Mater.* **2014**, *65*, 69.
[69] Y. Kang, K. Krishnaswamy, H. Peelaers, K. Ellmer, *J. Phys. D: Appl. Phys.* **2001**, *34*, 3097.
[70] W. H. Nam, Y. S. Lim, S. M. Choi, W. S. Seo, J. Y. Lee, *J. Mater. Chem.* **2012**, *22*, 14633.
[71] J. Nomoto, H. Makino, T. Yamamoto, *Thin Solid Films* **2017**, *644*, 33.
[72] N. P. Dasgupta, S. Neubert, W. Lee, O. Trejo, J. R. Lee, F. B. Prinz, *Chem. Mater.* **2010**, *22*, 4769.
[73] A. C. Marques, J. Faria, P. Perdigão, B. M. M. Faustino, R. Ritasalo, K. Costabello, R. C. da Silva, I. Ferreira, *Sci. Rep.* **2019**, *9*, article no. 17919.
[74] I. A. Tambasov, M. N. Volochaev, A. S. Voronin, N. P. Evsevskaya, A. N. Masyugin, A. S. Aleksandrovskii, T. E. Smolyarova, I. V. Nemtsev, S. A. Lyashchenko, G. N. Bondarenko, E. V. Tambasova, *Phys. Solid State* **2019**, *61*, 1904.
[75] N. W. Park, J. Y. Ahn, T. H. Park, J. H. Lee, W. Y. Lee, K. Cho, Y. G. Yoon, C. J. Choi, J. S. Park, S. K. Lee, *Nanoscale* **2017**, *9*, 7027.
[76] T. Tynell, I. Terasaki, H. Yamauchi, M. Karppinen, *J. Mater. Chem. A* **2013**, *1*, 13619.
[77] T. Koskinen, U. Volin, C. Tossi, R. Raju, I. Tittonen, *Nanotechnology* **2023**, *34*, 035401.
[78] N. H. Tran Nguyen, T. H. Nguyen, Y. R. Liu, M. Aminzare, A. T. T. Pham, S. Cho, D. P. Wong, K. H. Chen, T. Seetawan, N. K. Pham, H. K. T. Ta, V. C. Tran, T. B. Phan, *ACS Appl. Mater. Interfaces* **2016**, *8*, 33916.
[79] D. K. Seo, S. Shin, H. H. Cho, B. H. Kong, D. M. Whang, H. K. Cho, *Acta Mater.* **2011**, *59*, 6743.
[80] Z. H. Zheng, P. Fan, J. T. Luo, G. X. Liang, D. P. Zhang, *Electron. Mater. Lett.* **2015**, *11*, 429.
[81] M. V. Castro, M. F. Cerqueira, L. Rebouta, P. Alpuim, C. B. Garcia, G. L. Júnior, C. J. Tavares, *Vacuum* **2014**, *107*, 145.
[82] A. T. T. Pham, O. K. T. Le, T. T. T. Phan, D. Van Hoang, T. H. Nguyen, N. D. Le, T. B. Phan, V. C. Tran, *Vacuum* **2022**, *202*, 111137.
[83] A. T. T. Pham, O. K. T. Le, D. Van Hoang, T. H. Nguyen, K. H. Chen, S. Park, T. B. Phan, V. C. Tran, *Acta Mater.* **2022**, *241*, 118415.
[84] G. Li, S. Liu, Y. Piao, B. Jia, Y. Yuan, Q. Wang, *Mater. Des.* **2018**, *154*, 41.
[85] A. I. Abutaha, S. R. Sarath Kumar, H. N. Alshareef, *Appl. Phys. Lett.* **2013**, *102*, 053507.
[86] P. Mele, S. Saini, H. Honda, K. Matsumoto, K. Miyazaki, H. Hagino, A. Ichinose, *Appl. Phys. Lett.* **2013**, *102*, 253903.
[87] Z. Zhou, Y. Zheng, Y. Yang, W. Zhang, B. Wei, M. Zou, J. Lan, C. W. Nan, Y. H. Lin, *J. Am. Ceram. Soc.* **2023**, *106*, 2911.
[88] A. K. Ambedkar, M. Singh, V. Kumar, V. Kumar, B. P. Singh, A. Kumar, Y. K. Gautam, *Surf. Interfaces* **2020**, *19*, 100504.
[89] S. Liu, M. Lan, G. Li, Y. Piao, H. Ahmoum, Q. Wang, *Energy* **2021**, *225*, 120320.
[90] COMSOL Multiphysics, *COMSOL - Software for Multiphysics Simulation*, COMSOL AB, Stockholm, Sweden **2021**.
[91] D. Zappa, S. Dalola, G. Faglia, E. Comini, M. Ferroni, C. Soldano, V. Ferrari, G. Sberveglieri, *Beilstein J. Nanotechnol.* **2014**, *5*, 927.
[92] E. M. F. Vieira, J. P. B. Silva, K. Veltruská, C. M. Istrate, V. Lenzi, V. Trifiletti, B. Lorenzi, V. Matolín, C. Ghica, L. Marques, O. Fenwick, L. M. Goncalves, *ACS Appl. Mater. Interfaces* **2021**, *13*, 35187.
[93] N. Klochko, K. Klepikova, I. Khrypunova, V. Kopach, S. Petrushenko, D. Zhadan, S. Dukarov, V. Sukhov, M. Kirichenko, A. Khrypunova, *Mater. Today Proc.* **2022**, *62*, 5729.
[94] O. Y. Ramírez-Esquivel, D. A. Mazón-Montijo, D. Cabrera-German, E. Martínez-Guerra, Z. Montiel-González, *Ceram. Int.* **2021**, *47*, 7126.
[95] C. H. Ahn, B. H. Kong, H. Kim, H. K. Cho, *J. Electrochem. Soc.* **2011**, *158*, H170.
[96] Rigaku, *Rigaku J.* **2010**, *26*, 23.
[97] H. Schulz, K. H. Thiemann, *Solid State Commun.* **1979**, *32*, 783.
[98] Y. Sekimoto, R. Abe, H. Kojima, H. Benten, M. Nakamura, *J. Therm. Anal. Calorim.* **2023**, *148*, 2285.
[99] J. Loureiro, N. Neves, R. Barros, T. Mateus, R. Santos, S. Filonovich, S. Reparaz, C. M. Sotomayor-Torres, F. Wyczisk, L. Divay, R. Martins, I. Ferreira, *J. Mater. Chem. A* **2014**, *2*, 6649.


© 2023 The Authors. Small Structures published by Wiley-VCH GmbH

26884062, 0, Downloaded from https://onlinelibrary.wiley.com/doi/10.1002/sstr.202300140 by Test, Wiley Online Library on [26/07/2023]. See the Terms and Conditions (https://onlinelibrary.wiley.com/terms-and-conditions) on Wiley Online Library for rules of use; OA articles are governed by the applicable Creative Commons License